

Gerald Eigen,
representing the BABAR collaboration

Dept. of Physics, University of Bergen, Allegation 55, Bergen, Norway

E-mail: gerald.eigen@ift.uib.no

Abstract. We present herein the most recent *BABAR* results on direct *CP* asymmetry measurements in $B \rightarrow X_s \gamma$, on partial branching fraction and *CP* asymmetry measurements in $B \rightarrow X_s \ell^+ \ell^-$, on a search for $B \rightarrow \pi/\eta \ell^+ \ell^-$ decays, on a search for lepton number violation in $B^+ \rightarrow X^- \ell^+ \ell'^+$ modes and a study of $B^0 \rightarrow \omega \omega$ and $B^0 \rightarrow \omega \phi$ decays.

1. Introduction

The decays $B \rightarrow X_{s,d} \gamma$ and $B \rightarrow X_{s,d} \ell^+ \ell^-$ (with $\ell^+ \ell^- = e^+ e^-, \mu^+ \mu^-$) are flavor-changing neutral-current (FCNC) processes that are forbidden in the Standard Model (SM) at tree level. They occur in higher-order processes and are described by an effective Hamiltonian that factorizes short-distance contributions in terms of scale-dependent Wilson coefficients $C_i(\mu)$ [1] from long-distance contributions expressed by local four-fermion operators \mathcal{O}_i that define hadronic matrix elements,

$$H_{\text{eff}} = \frac{4G_F}{\sqrt{2}} \sum_i C_i(\mu) \mathcal{O}_i. \quad (1)$$

While Wilson coefficients are calculable perturbatively, the calculation of the hadronic matrix elements requires non-perturbative methods such as the heavy quark expansion [2–4].

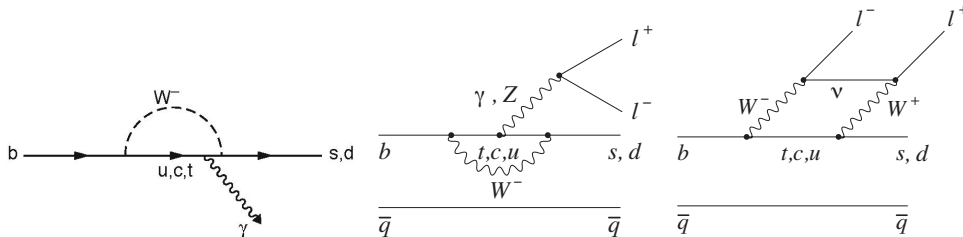


Figure 1. Lowest-order diagrams for $B \rightarrow X_{s,d} \gamma$ (left) and $B \rightarrow X_{s,d} \ell^+ \ell^-$ (middle, right).

Figure 1 shows the lowest order diagrams for these FCNC decays. In $B \rightarrow X_{s,d} \gamma$, the electromagnetic penguin loop dominates. The short-distance part is expressed by the effective Wilson coefficient C_7^{eff} . Through operator mixing at higher orders, the chromomagnetic penguin enters whose short distance part is parameterized by C_8^{eff} . In $B \rightarrow X_{s,d} \ell^+ \ell^-$ modes, the Z penguin and the WW box diagram contribute in addition whose short-distance parts are parametrized in terms of C_9^{eff} and C_{10}^{eff} , the vector and axial-vector current contributions of these diagrams. Physics beyond the SM introduces new loops and box diagrams with new particles (e.g. a charged Higgs boson or supersymmetric particles) as shown in Fig. 2 (left, middle). Such contributions modify the Wilson coefficients and may introduce new diagrams with scalar and pseudoscalar current interactions and in turn new Wilson coefficients, C_S and C_P [5]. To determine C_7^{eff} , C_8^{eff} , C_9^{eff} and C_{10}^{eff} precisely, we need to measure many observables in several radiative and rare semileptonic decays, which potentially can probe new physics at a scale of a few TeV.

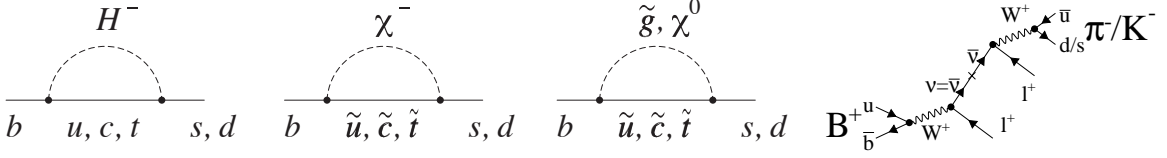


Figure 2. Examples of new physics processes via a charged Higgs boson (left), charginos (middle left), neutralinos (middle right) and via Majorana-type neutrino interactions (right).

Lepton-number-violating decays are highly suppressed in the SM and may need new physics processes. Figure 2 (right) shows a W annihilation diagram into $\ell^+\nu_\ell$ in which the neutrino mixes into an antineutrino producing like-sign leptons that are forbidden in SM interactions. Such processes require Majorana-type neutrinos that are absent in the SM [6].

The decays $B^0 \rightarrow \omega\omega$ and $B^0 \rightarrow \omega\phi$ also involve FCNC processes that are mediated by gluonic penguin loops included in H_{eff} (see Eqn. (1)). Here, the short-distance contributions are parameterized by the Wilson coefficients C_3, C_4, C_5 and C_6 , while the long-distance contributions involve the operators $\mathcal{O}_3, \mathcal{O}_4, \mathcal{O}_5$ and \mathcal{O}_6 . Figure 3 shows the lowest-order diagrams for these decays. New physics loops depicted in Fig. 2 may also contribute here. These charmless vector vector decays involve three amplitudes. In the transversity frame, these are the longitudinal amplitude A_0 (S-wave), the transverse amplitude A_T (P-wave) and the parallel amplitude $A_{||}$ (D-wave). For measuring CP violation, they need to be known.

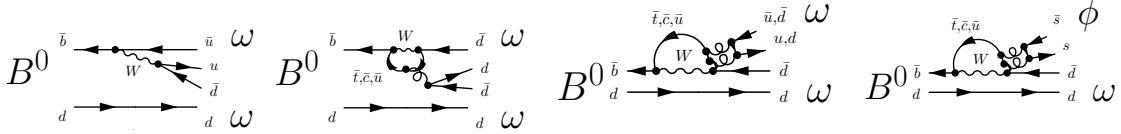


Figure 3. Lowest-order diagrams for the $B^0 \rightarrow \omega\omega$ color-suppressed tree (left), singlet penguin (middle left) and gluonic penguin (middle right) and the gluonic penguin for $B^0 \rightarrow \omega\phi$ (right).

In chapter 2, we present new *BABAR* measurements of the direct CP asymmetry in $B \rightarrow X_s\gamma$ using a semi-inclusive analysis. We extract the ratio of Wilson coefficients $\text{Im}(C_8^{\text{eff}}/C_7^{\text{eff}})$ from a measurement of the difference in CP asymmetries between charged and neutral B decays. We also show CP asymmetry measurements for $B \rightarrow X_{s,d}\gamma$ decays. In chapter 3, we present our branching fraction and CP asymmetry measurements of $B \rightarrow X_s\ell^+\ell^-$ decays using a semi-inclusive analysis. In chapter 4, we summarize our branching fraction upper limits on $B \rightarrow \pi\ell^+\ell^-$ and $B \rightarrow \eta\ell^+\ell^-$. In chapter 5, we summarize our results on searches for lepton number violation in exclusive $B^+ \rightarrow X^-\ell^+\ell'^+$ modes. In chapter 6, we present our results on the charmless vector vector decays $B^0 \rightarrow \omega\omega$ and $B^0 \rightarrow \omega\phi$ and in chapter 7 we end with concluding remarks. Note that *BABAR* performs all analyses blinded meaning that results are sealed until selection criteria and fitting procedures are finalized.

2. Measurement of CP Violation in $B \rightarrow X_s\gamma$

In the SM, the $B \rightarrow X_s\gamma$ branching fraction is calculated at next-to-next-to-leading order (up to four loops) yielding $\mathcal{B}(B \rightarrow X_s\gamma) = (3.14 \pm 0.22) \times 10^{-4}$ for photon energies $E_\gamma^* > 1.6$ GeV in the center-of-mass (CM) frame [7, 8]. For larger values of E_γ^* , the prediction depends the shape of the of the E_γ^* spectrum, which is modeled in terms of a shape function [9] that depends on the Fermi motion of the b quark inside the B meson and thus on the b quark mass. Since the shape function is expected to be similar to that determining the lepton-energy spectrum in $B \rightarrow X_u\ell\nu$, precision measurements of the E_γ^* spectrum help to determine $|V_{ub}|$ more precisely [10–12]. The measurement of $\mathcal{B}(B \rightarrow X_s\gamma)$ also provides constraints on the charged Higgs mass [13, 14].

Experimentally, the challenge consists of extracting $B \rightarrow X_s \gamma$ signal photons from those of π^0 and η decays, copiously produced in $q\bar{q}$ continuum (with $q = u, d, s, c$) and $B\bar{B}$ processes that increase exponentially at smaller photon energies. One strategy consists of summing $b \rightarrow s\gamma$ exclusive final states. In a sample of 471×10^{-6} $B\bar{B}$ events collected with the *BABAR* detector [15, 16] at the PEP-II asymmetric storage ring at the SLAC National Laboratory, we reconstruct 38 exclusive final states containing one or three kaons with at most one K_S^0 , up to four pions with at most two π^0 s and up to one η . We require photon energies in the CM frame of $1.6 < E_\gamma^* < 3.0$ GeV. Previously, we published total and partial branching fractions [17]. Here, we focus on the measurement of direct CP asymmetry, which is defined by

$$\mathcal{A}_{CP}(B \rightarrow X_s \gamma) \equiv \frac{\mathcal{B}(\bar{B} \rightarrow \bar{X}_s \gamma) - \mathcal{B}(B \rightarrow X_s \gamma)}{\mathcal{B}(\bar{B} \rightarrow \bar{X}_s \gamma) + \mathcal{B}(B \rightarrow X_s \gamma)}. \quad (2)$$

For this analysis [18], we select 16 self-tagging modes, ten $B^+ \rightarrow h^+ \gamma^1$ and six $B^0 \rightarrow h^0 \gamma$ final states². We maximize the signal extraction using a bagged decision tree with six input variables. This improves the efficiency considerably with respect to the standard $\Delta E = E_B^* - E_{beam}^*$ selection where E_{beam}^* and E_B^* are the beam energy and B meson energy in the CM frame, respectively. To remove continuum background, we train a separate bagged decision tree using event shape variables. For each X_s mass bin, we optimize the sensitivity $S/\sqrt{(S+B)}$ where $S(B)$ is the signal (background) yield using loosely identified pions and kaons. To extract \mathcal{A}_{CP} , we fit the beam-energy-constrained mass $m_{ES} = \sqrt{E_{beam}^{*2} - p_B^{*2}}$ simultaneously for \bar{B} -tagged and B -tagged events where p_B^* is the B momentum in the CM frame. After correcting the raw \mathcal{A}_{CP} for detector bias determined from the m_{ES} sideband below the signal region, we measure $\mathcal{A}_{CP}(B \rightarrow X_s \gamma) = (1.73 \pm 1.93_{stat} \pm 1.02_{sys})\%$ [18], which agrees well with the SM prediction of $-0.6\% < \mathcal{A}_{CP} < 2.8\%$ at 95% confidence level (CL) [19] and which supersedes the old *BABAR* measurement [20]. Though this result is the most precise single direct \mathcal{A}_{CP} measurement, the uncertainty is sufficiently large to allow for new physics contributions in C_7^{eff} . Figure 4 (bottom part) shows our result [18] in comparison to the Belle measurement [21]. The CP asymmetry difference between B^+ and B^0 decays, $\Delta\mathcal{A}_{CP}(B \rightarrow X_s \gamma) = \mathcal{A}_{CP}(B^+ \rightarrow X_s^+ \gamma) - \mathcal{A}_{CP}(B^0 \rightarrow X_s^0 \gamma)$, is very sensitive to new physics since it originates from the interference between the electromagnetic and the chromomagnetic penguin diagrams in which the latter enters through higher-order corrections. Calculations yield [19]

$$\Delta\mathcal{A}_{CP}(B \rightarrow X_s \gamma) \simeq 4\pi^2 \alpha_s \frac{\bar{\Lambda}_{78}}{m_b} \mathcal{I}m \frac{C_8^{eff}}{C_7^{eff}} \simeq 0.12 \frac{\bar{\Lambda}_{78}}{100 \text{ MeV}} \mathcal{I}m \frac{C_8^{eff}}{C_7^{eff}}, \quad (3)$$

where $\bar{\Lambda}_{78}$ is the hadronic matrix element of the $\mathcal{O}_7 - \mathcal{O}_8$ interference, predicted to lie in the range $17 \text{ MeV} < \bar{\Lambda}_{78} < 190 \text{ MeV}$. In the SM, $\Delta\mathcal{A}_{CP}(B \rightarrow X_s \gamma)$ vanishes since C_7^{eff} and C_8^{eff} are real. However in new physics models, these Wilson coefficients may have imaginary parts yielding non-vanishing $\Delta\mathcal{A}_{CP}(B \rightarrow X_s \gamma)$ [22–24]. From a simultaneous fit to B^+ and B^0 modes, we measure $\Delta\mathcal{A}_{CP}(B \rightarrow X_s \gamma) = (5.0 \pm 3.9_{stat} \pm 1.5_{sys})\%$ from which we obtain the constraint $-1.64 < \mathcal{I}m(C_8^{eff}/C_7^{eff}) < 6.52$ at 90% CL. This is the first $\Delta\mathcal{A}_{CP}(B \rightarrow X_s \gamma)$ measurement and first constraint on $\mathcal{I}m(C_8^{eff}/C_7^{eff})$.

Figure 5 (left) shows the $\Delta\chi^2$ of the fit as a function of $\mathcal{I}m(C_8^{eff}/C_7^{eff})$. The $\Delta\chi^2$ dependence on $\mathcal{I}m(C_8^{eff}/C_7^{eff})$ is not parabolic indicating that the likelihood has a non-Gaussian shape. The reason is that $\Delta\chi^2$ is determined from all possible values of $\bar{\Lambda}_{78}$. In the region $0.2 < \mathcal{I}m(C_8^{eff}/C_7^{eff}) < 2.6$, a change in $\mathcal{I}m(C_8^{eff}/C_7^{eff})$ can be compensated by a change in $\bar{\Lambda}_{78}$ leaving $\Delta\chi^2$ unchanged. For positive values larger (smaller) than 2.6 (0.2), $\Delta\chi^2$ increases slowly

¹ $h^+ = K_S^0 \pi^+, K^+ \pi^0, K^+ \pi^+ \pi^-, K_S^0 \pi^+ \pi^0, K^+ \pi^0 \pi^0, K_S^0 \pi^+ \pi^- \pi^+, K^+ \pi^+ \pi^- \pi^0, K_S^0 \pi^+ \pi^0 \pi^0, K^+ \eta, K^+ K^+ K^-$.

² $h^0 = K^+ \pi^-, K^+ \pi^- \pi^0, K^+ \pi^+ \pi^- \pi^-, K^+ \pi^- \pi^0 \pi^0, K^+ \pi^- \eta, K^+ K^+ K^- \pi^-$.

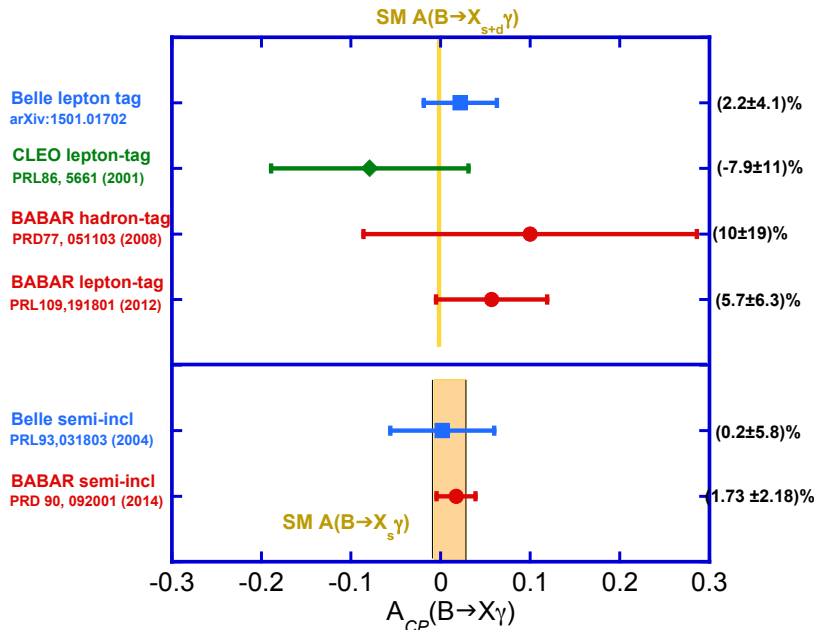


Figure 4. Summary of \mathcal{A}_{CP} measurements for $B \rightarrow X_s \gamma$ from semi-inclusive analyses (bottom part) from BABAR [18] and Belle [21] and for $B \rightarrow X_{s+d} \gamma$ from fully inclusive analyses (top part) from BABAR [25–27], Belle [28] and CLEO [29] in comparison to the SM prediction for $B \rightarrow X_s \gamma$ [19] and for $B \rightarrow X_{s,d} \gamma$ [22, 30], respectively.

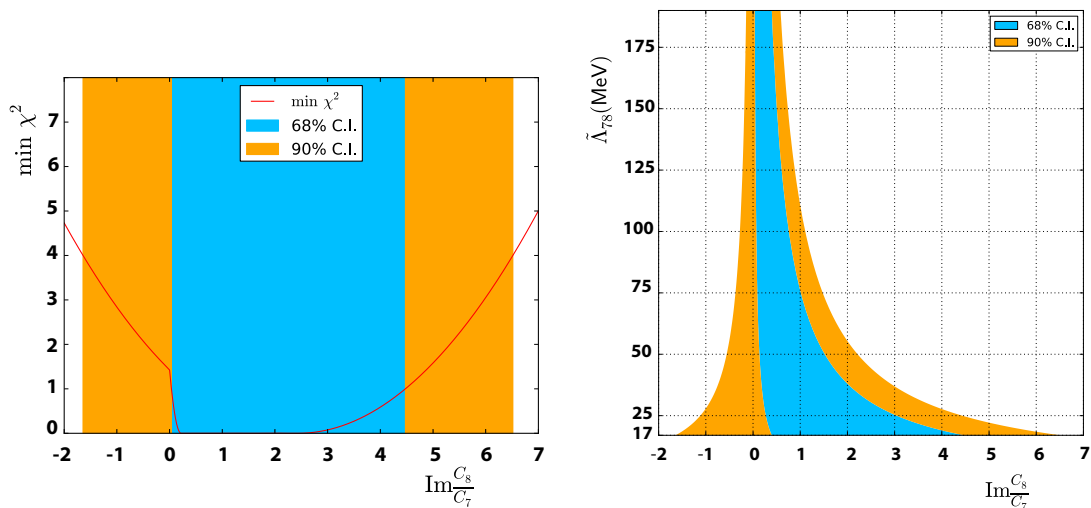


Figure 5. The $\Delta\chi^2$ (left) and $\bar{\Lambda}_{78}$ (right) dependence on $\text{Im}(C_8^{\text{eff}}/C_7^{\text{eff}})$. The blue dark-shaded (orange light-shaded) region shows the 68% (90%) CL interval.

(rapidly) since $\bar{\Lambda}_{78}$ remains nearly constant at the minimum value (increases rapidly). For negative $\text{Im}(C_8^{\text{eff}}/C_7^{\text{eff}})$ values, $\bar{\Lambda}_{78}$ starts to decrease again, which leads to a change in the $\Delta\chi^2$ shape. Figure 5 (right) shows $\bar{\Lambda}_{78}$ as a function of $\text{Im}(C_8^{\text{eff}}/C_7^{\text{eff}})$.

In the fully inclusive analysis, \mathcal{A}_{CP} involves contributions from $B \rightarrow X_s \gamma$ and $B \rightarrow X_d \gamma$ that cannot be separated on an event-by-event basis. Therefore, we define \mathcal{A}_{CP} here as

$$\mathcal{A}_{CP}(B \rightarrow X_{s+d}\gamma) \equiv \frac{\mathcal{B}(\bar{B} \rightarrow X_{s+d}\gamma) - \mathcal{B}(B \rightarrow X_{s+d}\gamma)}{\mathcal{B}(\bar{B} \rightarrow X_{s+d}\gamma) + \mathcal{B}(B \rightarrow X_{s+d}\gamma)}. \quad (4)$$

We tag the flavor of the non-signal \bar{B} flavor by the lepton charge in semileptonic decays. Using a sample 384×10^6 $B\bar{B}$ events, we measure $\mathcal{A}_{CP}(B \rightarrow X_{s+d}\gamma) = 0.057 \pm 0.06_{stat} \pm 0.018_{sys}$ after correcting for charge bias and mistagging [17]. Figure 4 (top part) shows all $\mathcal{A}_{CP}(B \rightarrow X_{s+d}\gamma)$ measurements from *BABAR* [25–27], *Belle* [28] and *CLEO* [29], which all agree well with the SM prediction [22, 30].

3. Study of $B \rightarrow X_s \ell^+ \ell^-$ Decays

Using a semi-inclusive approach, we have updated the partial and total branching fraction measurements of $B \rightarrow X_s \ell^+ \ell^-$ modes ($\ell = e$ or μ) with the full *BABAR* data sample of 471×10^6 $B\bar{B}$ events. We reconstruct 20 exclusive final states: K^+ , K_S^0 , $K^{*+}(K^+\pi^0, K_S^0\pi^+)$, $K^{*0}(K^+\pi^-, K_S^0\pi^0)$, $K^+\pi^-\pi^0$, $K_S^0\pi^+\pi^-$ with $K_S^0 \rightarrow \pi^+\pi^-$ recoiling against e^+e^- or $\mu^+\mu^-$ [31]. After accounting for K_L^0 modes, $K_S^0 \rightarrow \pi^0\pi^0$ and π^0 Dalitz decays, the selected decay modes represent 70% of the inclusive rate for hadronic masses $m_{X_s} < 1.8$ GeV/ c^2 . Using JETSET fragmentation [32] and theory predictions [33–38], we extrapolate for the missing modes and those with $m_{X_s} > 1.8$ GeV/ c^2 . We impose the requirements $m_{ES} > 5.225$ GeV/ c^2 and 0.1 (0.05) $< \Delta E < 0.05$ (0.05) GeV for $X_s e^+e^-$ ($X_s \mu^+\mu^-$) modes. We define six bins of the momentum-squared transferred to the dilepton system $q^2 = m_{\ell\ell}^2$ and four bins in hadronic mass m_{X_s} . Table 1 shows the defined ranges of these bins.

Table 1. Definition of the q^2 , $m_{\ell\ell}$ and m_{X_s} bins.

q^2 bin	q^2 range [GeV ² / c^4]	$m_{\ell\ell}$ range [GeV/ c^2]	m_{X_s} bin	m_{X_s} range [GeV/ c^2]
0	1.0 – 6.0	1.00 – 2.45		
1	0.1–2.0	0.32– 1.41	1	0.4 – 0.6
2	2.0–4.3	1.41–2.07	2	0.6 –1.0
3	4.3–8.1	2.07 –2.6	3	1.0 –1.4
4	10.1 –12.9	3.18–3.59	4	1.4 – 1.8
5	$14.2 - (m_B - m_K^*)^2$	$3.77 - (m_B - m_K^*)$		

To suppress $e^+e^- \rightarrow q\bar{q}$ and $B\bar{B}$ combinatorial background, we define boosted decision trees (BDT) for each q^2 bin separately for e^+e^- and $\mu^+\mu^-$ modes. From these BDTs, we determine a likelihood ratio (L_R) to separate signal from $q\bar{q}$ and $B\bar{B}$ backgrounds. We veto J/ψ and $\psi(2S)$ mass regions and use them as control samples. We measure $d\mathcal{B}(B \rightarrow X_s \ell^+ \ell^-)/dq^2$ in six bins of q^2 and four bins of m_{X_s} . We extract the signal in each bin from a two-dimensional fit to m_{ES} and L_R . As examples, Figs. 6 and 7 show the m_{ES} and L_R distributions for e^+e^- modes in bin q_5 and for $\mu^+\mu^-$ modes in bin q_1 , respectively. Clear signals are visible both in the m_{ES} and L_R distributions. Figure 8 shows the differential branching fraction as a function of q^2 (left) and m_{X_s} (right) [31]. Table 2 summarizes the differential branching fractions in the low and high q^2 regions in comparison to the SM predictions [34, 38–47]. In both q^2 regions, the differential branching fractions are in good agreement with the SM predictions. These results supersede the previous *BABAR* measurements [48] and agree well with the measurements from *Belle* [49].

The direct CP asymmetry is defined by

$$\mathcal{A}_{CP} = \frac{\mathcal{B}(\bar{B} \rightarrow \bar{X}_s \ell^+ \ell^-) - \mathcal{B}(B \rightarrow X_s \ell^+ \ell^-)}{\mathcal{B}(\bar{B} \rightarrow \bar{X}_s \ell^+ \ell^-) + \mathcal{B}(B \rightarrow X_s \ell^+ \ell^-)}. \quad (5)$$

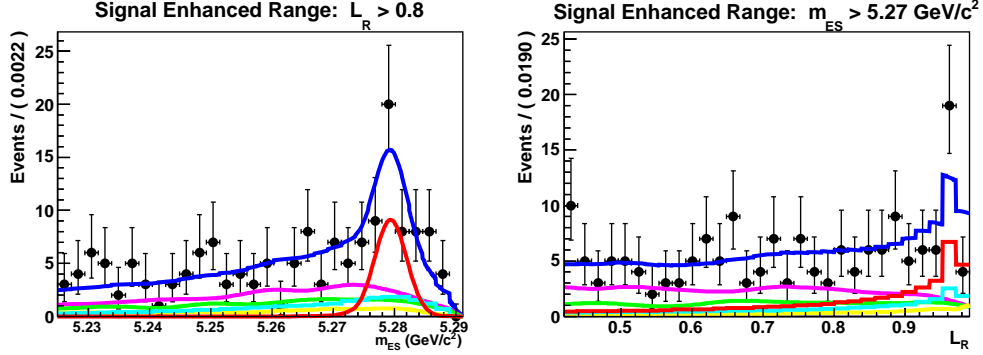


Figure 6. Distributions of m_{ES} (left) and likelihood ratio (right) for $B \rightarrow X_s e^+ e^-$ in q^2 bin q_5 showing data (points with error bars), the total fit (thick solid blue curves), signal component (red peaking curves), signal cross feed (cyan curves), $B\bar{B}$ background (magenta curve), $e^+e^- \rightarrow q\bar{q}$ background (green curves) and charmonium background (yellow curves).

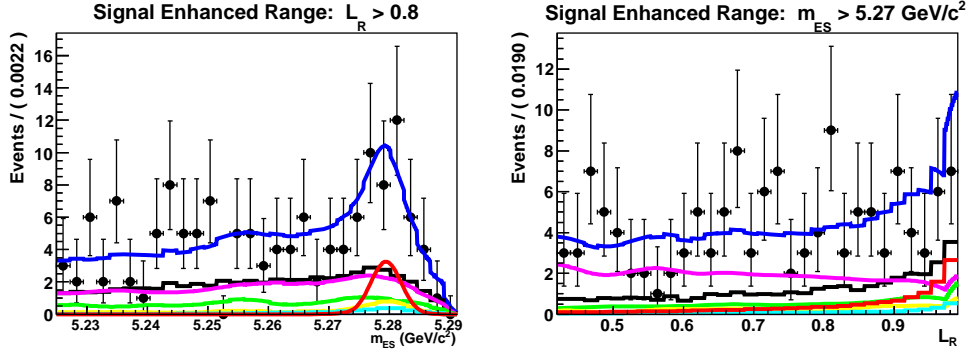


Figure 7. Distributions of m_{ES} (left) and likelihood ratio (right) for $B \rightarrow X_s \mu^+ \mu^-$ in q^2 bin q_1 showing data (points with error bars), the total fit (thick solid blue curves), signal component (red peaking curves), signal cross feed (cyan curves), $B\bar{B}$ background (magenta curve), $e^+e^- \rightarrow q\bar{q}$ background (green curves) and charmonium background (yellow curves).

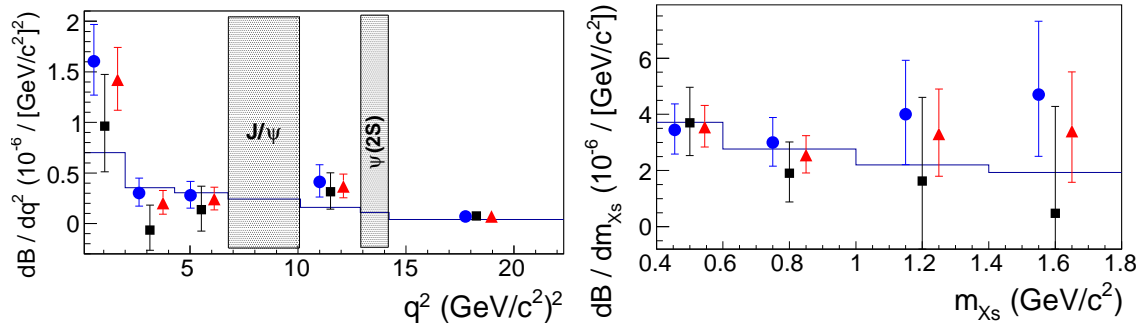


Figure 8. Differential branching fraction of $B \rightarrow X_s e^+ e^-$ (blue points), $B \rightarrow X_s \mu^+ \mu^-$ (black squares) and $B \rightarrow X_s \ell^+ \ell^-$ (red triangles) versus q^2 (top) and versus m_{X_s} (bottom) in comparison to the SM prediction (histogram). Grey-shaded bands show J/ψ and $\psi(2S)$ vetoed regions.

Table 2. Measured $B \rightarrow X_s \ell^+ \ell^-$ branching fractions in the low and high q^2 regions from BABAR [31] and the SM predictions. Uncertainties are statistical, systematic and from model dependence, respectively.

Mode	BABAR [10^{-6}]	SM [10^{-6}]	BABAR [10^{-6}]	SM [10^{-6}]
$q^2 [\text{GeV}^2/c^4]$	1 – 6	1 – 6	> 14.2	> 14.2
$B \rightarrow X_s \mu^+ \mu^-$	$0.66^{+0.82+0.30}_{-0.76-0.24} \pm 0.07$	1.59 ± 0.11	$0.60^{+0.31+0.05}_{-0.29-0.04} \pm 0.00$	$0.25^{+0.07}_{-0.06}$
$B \rightarrow X_s e^+ e^-$	$1.93^{+0.47+0.21}_{-0.45-0.16} \pm 0.18$	1.64 ± 0.11	$0.56^{+0.19+0.03}_{-0.18-0.03} \pm 0.00$	$0.25^{+0.07}_{-0.06}$
$B \rightarrow X_s \ell^+ \ell^-$	$1.60^{+0.41+0.17}_{-0.39-0.13} \pm 0.07$		$0.57^{+0.16+0.03}_{-0.15-0.02} \pm 0.00$	$0.25^{+0.07}_{-0.06}$

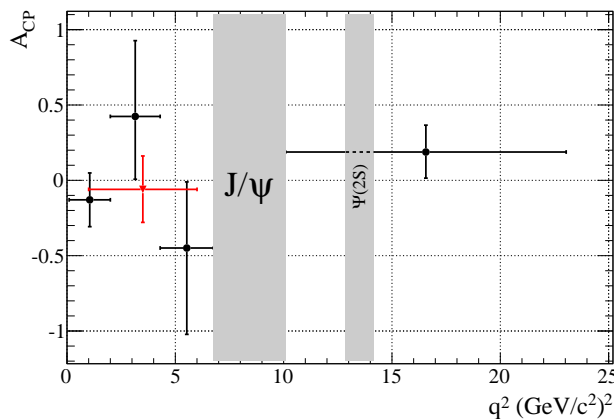


Figure 9. The CP asymmetry versus q^2 . Grey bands show the J/ψ and $\psi(2S)$ vetoed regions.

We use 14 self-tagging modes consisting of all B^+ modes and B^0 modes with decays to a K^+ to measure $\mathcal{A}_{CP}(B \rightarrow X_s \ell^+ \ell^-)$ in five q^2 bins. Due to low statistics, we have combined bins q_4 and q_5 . Figure 9 shows the CP asymmetry as a function of q^2 . The SM prediction of the CP asymmetry in the entire q^2 region is close to zero [50–53]. In new physics models, however, \mathcal{A}_{CP} may be significantly enhanced [54, 55]. In the full range of q^2 , we measure $\mathcal{A}_{CP}(B \rightarrow X_s \ell^+ \ell^-) = 0.04 \pm 0.11_{stat} \pm 0.01_{sys}$ [31], which is in good agreement with the SM prediction. The CP asymmetries in the five q^2 bins are also consistent with zero.

4. Search for $B \rightarrow \pi/\eta \ell^+ \ell^-$ Decays

In the SM in lowest order, $B \rightarrow X_d \ell^+ \ell^-$ modes are also mediated by the electromagnetic penguin, Z penguin and WW box diagrams. However, they are suppressed by $|V_{td}/V_{ts}|^2 \simeq 0.04$ with respect to the corresponding $B \rightarrow X_s \ell^+ \ell^-$ decays. In extensions of the SM, rates may increase significantly [56]. Using $471 \times 10^6 B\bar{B}$ events, we recently updated the search for $B \rightarrow \pi \ell^+ \ell^-$ modes and performed the first search for $B \rightarrow \eta \ell^+ \ell^-$ modes [57]. The SM predictions lie in the range $\mathcal{B}(B \rightarrow \pi \ell^+ \ell^-) = (1.96\text{--}3.30) \times 10^{-8}$ and $\mathcal{B}(B \rightarrow \eta \ell^+ \ell^-) = (2.5\text{--}3.7) \times 10^{-8}$ where the large ranges result from uncertainties in the $B \rightarrow \pi$ form factor calculations [56, 58, 59] and from a lack of knowledge of $B \rightarrow \eta$ form factors [60], respectively.

We fully reconstruct four $B \rightarrow \pi \ell^+ \ell^-$ and four $B \rightarrow \eta \ell^+ \ell^-$ final states by selecting $\pi^\pm, \pi^0 \rightarrow \gamma\gamma$ and $\eta \rightarrow \gamma\gamma, \pi^+\pi^-\pi^0$ recoiling against e^+e^- or $\mu^+\mu^-$. We select leptons with $p_\ell > 0.3 \text{ GeV}/c$, recover e^\pm bremsstrahlung losses, remove γ conversions and require good particle identification

for e^\pm , μ^\pm and π^\pm . We select photons with $E_\gamma > 50$ MeV and impose π^0 and η mass constraints of $115 < m_{\gamma\gamma} < 150$ MeV/ c^2 and 500 (535) $< m_{\gamma\gamma}$ ($m_{3\pi}$) < 575 (565) MeV/ c^2 , respectively. For the $\eta \rightarrow \gamma\gamma$ final state, we require $(E_{1,\gamma} - E_{2,\gamma})/(E_{1,\gamma} + E_{2,\gamma}) < 0.8$ to remove asymmetric $q\bar{q}$ background that peaks near one. We veto J/ψ and $\psi(2S)$ mass regions and use four neural networks (NN) to suppress combinatorial $B\bar{B}$ and $q\bar{q}$ continuum backgrounds, separately for e^+e^- and for $\mu^+\mu^-$ modes. The NNs for suppressing $B\bar{B}$ background use 15 (14) input distributions for e^+e^- ($\mu^+\mu^-$) modes, while those for suppressing $q\bar{q}$ continuum use 16 input distributions for both modes. For validations of the fitting procedure and peaking backgrounds, we use pseudo-experiments and the vetoed J/ψ and $\psi(2S)$ samples.

For $B^+ \rightarrow \pi^+\ell^+\ell^-$ and $B^0 \rightarrow \pi^0\ell^+\ell^-$, we perform simultaneous unbinned maximum likelihood (ML) fits to m_{ES} and ΔE distributions for e^+e^- and $\mu^+\mu^-$ modes separately. We include the $B^+ \rightarrow K^+\ell^+\ell^-$ mode in the fit to extract the peaking background contribution in the $B^+ \rightarrow \pi^+\ell^+\ell^-$ modes by reconstructing the K^+ as a π^+ . For $B^0 \rightarrow \eta\ell^+\ell^-$, we perform simultaneous unbinned ML fits to m_{ES} and ΔE distributions, again for e^+e^- and $\mu^+\mu^-$ modes separately. In addition, we perform fits for the isospin-averaged modes $B \rightarrow \pi e^+e^-$ and $B \rightarrow \pi\mu^+\mu^-$, lepton-flavor-averaged modes $B^+ \rightarrow \pi^+\ell^+\ell^-$, $B^0 \rightarrow \pi^0\ell^+\ell^-$ and $B^0 \rightarrow \eta\ell^+\ell^-$ and both isospin- and lepton-flavor-averaged modes $B \rightarrow \pi\ell^+\ell^-$.

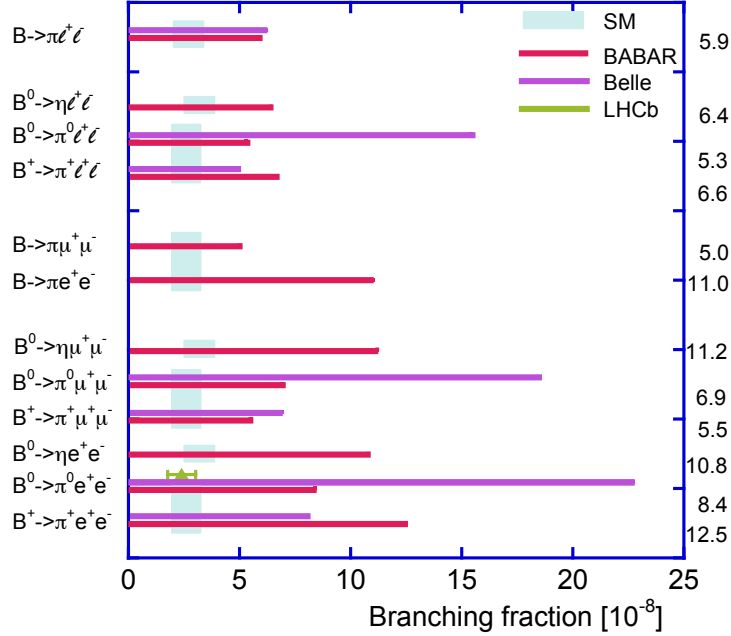


Figure 10. Branching fraction upper limits at 90% CL for $B \rightarrow \pi\ell^+\ell^-$ and $B \rightarrow \eta\ell^+\ell^-$ modes from BABAR [57] and Belle [61] and the measurement of $B^+ \rightarrow \pi^+\ell^+\ell^-$ from LHCb [62].

We see no signals in any of these modes and set branching fraction upper limits at 90% CL. Figure 10 shows them in comparison to results from Belle [61] and a measurement of $\mathcal{B}(B^+ \rightarrow \pi^+\mu^+\mu^-)$ from LHCb [62]. For $B^0 \rightarrow \pi^0\ell^+\ell^-$, our branching fraction upper limit is the lowest and so far only BABAR has searched for $B^0 \rightarrow \eta\ell^+\ell^-$ modes. The present branching fraction upper limits lie within a factor of two to three of the SM predictions.

5. Search for Lepton Number Violation in $B^+ \rightarrow X^-\ell^+\ell^+$ Decays

In the SM, lepton number is conserved in low-energy collisions. However, in high-energy and high-density interactions, lepton number may be violated [63]. Many models beyond the SM

predict lepton number violation (LNV) with rates [64] that may be accessible already in present data samples. These models also predict Majorana-type neutrinos [6] for which particles and antiparticles are identical. Via oscillation of a neutrino into an antineutrino, lepton-number violating decays become possible such as $B^+ \rightarrow K^- \ell^+ \ell'^-$ depicted in Fig. 2 (right). The observation of atmospheric neutrino oscillations confirms that neutrinos carry mass [65] but we do not know if any Majorana-type neutrinos exist. However, lepton number violation is also a necessary condition to explain the observed baryon asymmetry in the universe [66].

Using the full *BABAR* data set of 471×10^6 $B\bar{B}$ events collected at the $\Upsilon(4S)$ peak, we have searched for lepton number violation in 11 B^+ decays³ [67]. We select events with more than three charged tracks of which two are identified as like-sign leptons having a combined momentum less than 2.5 GeV/c in the laboratory frame. We remove e^+ and e^- from photon conversions. We define sufficiently wide mass regions around the ρ^- ($0.47 < m_{\pi\pi^0} < 1.07$ GeV/c²), K^{*-} ($0.770 < m_{K\pi} < 1.01$ GeV/c²) and D^- ($1.835 < m_{K\pi\pi} < 1.895$ GeV/c²) mesons to allow reasonable modeling of backgrounds. We combine the π^- , K^- , $\pi^-\pi^0$, $K^-\pi^0$, $K_S^0\pi^-$ and $K^-\pi^+\pi^-$ candidates with the two leptons to form a B candidate. We remove $\ell^\pm h^\mp$ combinations with an invariant mass close to that of the J/ψ as the h^\mp may be a misidentified μ^\mp from $J/\psi \rightarrow \mu^+\mu^-$. The misidentification rate is about 2%.

Table 3. Summary of signal yield after fit bias correction with statistical uncertainty, reconstruction efficiency ϵ , significance S including systematic error, measured branching fraction $\mathcal{B} \times 10^7$ and the 90% CL upper limit $\mathcal{B}_{UL} \times 10^7$. Yields and efficiencies for the $B^+ \rightarrow K^{*-} \ell^+ \ell'^+$ modes are for $K^-\pi^0$ and $K_S^0\pi^-$ final states, respectively.

Mode	Yield	ϵ	S	\mathcal{B}	\mathcal{B}_{UL}
	[events]	[%]	[σ]	[10^{-7}]	[10^{-7}]
$K^{*-} e^+ e^+$	$3.8 \pm 3.3, 0.8 \pm 3.9$	$11.5 \pm 0.1, 12.1 \pm 0.1$	1.2	$1.7 \pm 1.4 \pm 0.1$	4.0
$K^{*-} e^+ \mu^+$	$-1.9 \pm 4.7, -5.1 \pm 2.6$	$7.9 \pm 0.1, 8.5 \pm 0.1$	0.0	$-4.5 \pm 2.6 \pm 0.4$	3.0
$K^{*-} \mu^+ \mu^+$	$2.3 \pm 1.8, 2.0 \pm 1.8$	$6.1 \pm 0.1, 5.8 \pm 0.1$	1.3	$2.4 \pm 1.8 \pm 0.4$	5.9
$\rho^- e^+ e^+$	-2.1 ± 5.7	12.1 ± 0.1	0.0	$-0.4 \pm 1.0 \pm 0.1$	1.7
$\rho^- e^+ \mu^+$	4.6 ± 11.4	10.3 ± 0.1	0.4	$1.0 \pm 2.4 \pm 0.2$	4.7
$\rho^- \mu^+ \mu^+$	2.9 ± 6.8	7.3 ± 0.1	0.5	$0.9 \pm 2.0 \pm 0.3$	4.2
$D^- e^+ e^+$	3.9 ± 4.8	10.2 ± 0.1	1.0	$8.8 \pm 8.6 \pm 1.5$	26
$D^- e^+ \mu^+$	1.1 ± 3.2	7.7 ± 0.1	0.5	$3.4 \pm 9.4 \pm 1.1$	21
$D^- \mu^+ \mu^+$	-1.7 ± 2.5	5.7 ± 0.1	0.0	$-6.5 \pm 9.9 \pm 0.9$	17
$K^- e^+ \mu^+$	5.5 ± 3.5	15.2 ± 0.1	1.8	$0.6 \pm 0.5 \pm 0.1$	1.6
$\pi^- e^+ \mu^+$	3.8 ± 3.5	16.4 ± 0.2	1.2	$0.5 \pm 0.5 \pm 0.1$	1.5

For each signal mode, we construct BDTs to discriminate signal from $B\bar{B}$ and $q\bar{q}$ backgrounds using nine inputs consisting of event shape variables, kinematic observables, flavor tagging and the proper decay time. If more than one candidate is found, we choose the one with the smallest χ^2 in the fit to the B decay vertex. We perform a simultaneous unbinned ML fit

³ $B^+ \rightarrow \rho^-(\pi^-\pi^0)\ell^+\ell'^+$, $B^+ \rightarrow K^{*-}(K_S^0\pi^- \text{ and } K^-\pi^0)\ell^+\ell'^+$, $B^+ \rightarrow D^-(K^-\pi^+\pi^-)\ell^+\ell'^+$, $B^+ \rightarrow \pi^- e^+ \mu^+$ and $B^+ \rightarrow \pi^- e^+ \mu^+$ where $\ell^+, \ell'^+ = e^+$ or μ^+ .

to m_{ES} , ΔE and the BDT output distributions. For the $B^+ \rightarrow \rho^- \ell^+ \ell'^+$, $B^+ \rightarrow K^{*-} \ell^+ \ell'^+$ and $B^+ \rightarrow D^- \ell^+ \ell'^+$ final states, we include the $m_{\pi\pi}$, $m_{K\pi}$ and $m_{K\pi\pi}$ mass distributions, respectively. The background PDFs consist of an Argus function [68] for m_{ES} , first- or second-order polynomials (for K^- , π^- , ρ^- , K^{*-} modes) or a Cruijff⁴ function (for D^- modes) for ΔE , a non-parametric kernel estimation KEYS algorithm [69] for the BDT output and a first-order polynomial plus a Gaussian function for the resonance masses. The corresponding signal PDFs consist of a Crystal Ball function [70] for m_{ES} , a Crystal Ball function plus a first-order polynomial (for modes with π^0 s) for ΔE , the simulated distribution in form of a histogram for the BDT output and for the D , K^* , ρ masses two Gaussians, a relativistic Breit-Wigner function and a Gounaris-Sakurai function [71], respectively. We checked the fit procedure with a simulated background sample having the same size as the on-resonance data sample. We further performed a blinded fit to the on-resonance data sample confirming that the background distributions agreed with the background PDFs. Selection efficiencies vary between 6% and 16% depending on the final state.

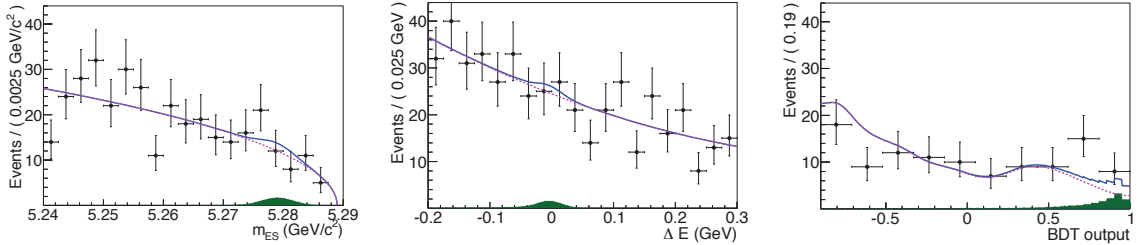


Figure 11. Projections of the multidimensional fit onto m_{ES} (left), ΔE (middle) and the BDT output (right) for $B^+ \rightarrow \pi^- e^+ \mu^+$ showing data (points with error bars), total fit (solid blue line), signal PDF (green histogram) and background (dashed magenta line).

Figures 11 and 12 show projections of the fit on the discriminating variables for $B^+ \rightarrow \pi^- e^+ \mu^+$ and $B^+ \rightarrow K^{*-} (K_S^0 \pi^-) \mu^+ \mu^+$, respectively. Table 3 summarizes our results. In all 11 modes, the data are consistent with combinatorial background. We see the highest significance of 1.8σ in $B^+ \rightarrow K^- e^+ \mu^+$. We set Bayesian upper limits on the branching fraction at 90% CL using a flat prior (see Tab. 3). The additive systematic uncertainty that includes contributions from the PDF parameterization, fit biases, background yields and efficiencies is mode dependent between 0.2 and 0.7 events. The total multiplicative uncertainty on the branching fraction is 5% or less. The branching fraction upper limits at 90% CL lie in the range $1.5 - 26 \times 10^{-7}$ where the lowest limit is set in the $B^+ \rightarrow \pi^- e^+ \mu^+$ mode. Figure 13 summarizes all results of lepton-number-violating B decays from BABAR [67], Belle [72], LHCb [73] and CLEO [74] including results for $B^0 \rightarrow \Lambda_c^+ \ell^-$, $B^- \rightarrow \Lambda \ell^-$, $B^- \rightarrow \bar{\Lambda} \ell^-$ [75] and $B^- \rightarrow \pi^- / K^- \ell^+ \ell^+$ [76]. All limits are set at 90% CL except for LHCb whose limits are set at 95% CL.

6. Study of $B^0 \rightarrow \omega\omega$ and $B^0 \rightarrow \omega\phi$ Decays

The longitudinal polarization fraction \mathcal{F}_L in charmless vector vector decays poses a puzzle. In tree-dominated decays like $B^0 \rightarrow \rho^+ \rho^-$ and $B^+ \rightarrow \rho^+ \rho^0$, \mathcal{F}_L is nearly 100% while in decays with dominant penguin contributions like $B \rightarrow K^* \rho$, \mathcal{F}_L is around 50% [77]. Are there large transverse SM contributions that reduce \mathcal{F}_L [78–83] or is this caused by new physics [82, 84–94]? Thus, it is interesting to investigate other charmless vector vector decays such as the so far not-observed modes $B^0 \rightarrow \omega\omega$ and $B^0 \rightarrow \omega\phi$ [95]. In the SM, the branching fractions are expected

⁴ The Cruijff function is a centered Gaussian with different left-right resolutions and non-Gaussian tails: $f(x) = \exp((x - m)^2 / (2\sigma_{L,R}^2 + \alpha_{L,R}(x - m)^2))$.

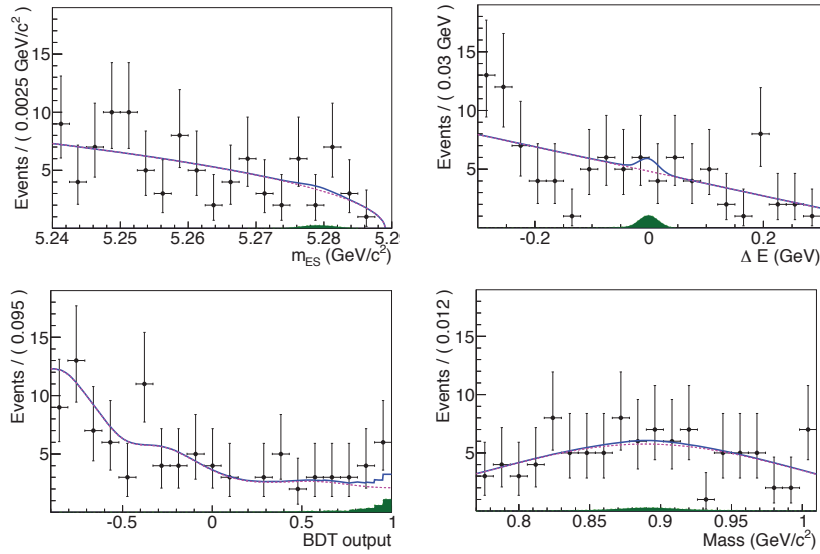


Figure 12. Projections of the multidimensional fit onto m_{ES} (top left), ΔE (top right), the BDT output (bottom left) and K^{*-} mass (bottom right) for $B^+ \rightarrow K^{*-} (K_S^0 \pi^-) e^+ \mu^+$ showing data (points with error bars), total fit (solid blue line), signal PDF (green histogram) and background (dashed magenta line).

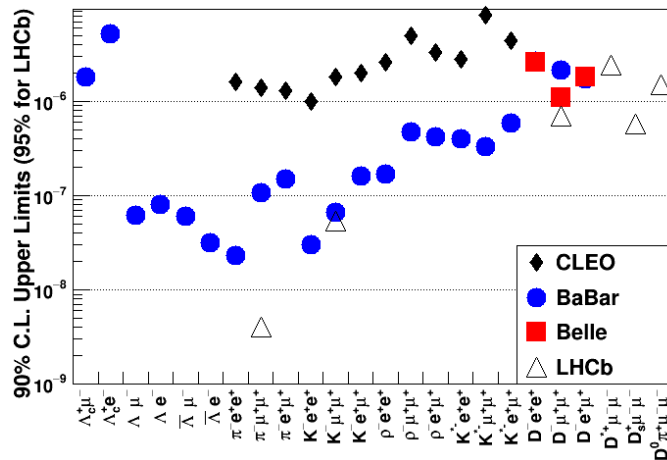


Figure 13. Branching fraction upper limits at 90% CL for LNV decays from BABAR [67] (solid blue points), Belle [72] (solid red squares) and CLEO [74] (black diamonds). In addition, LHCb upper limits at 95% CL [73] (open triangles) are shown.

to be of the order of $\mathcal{O}(10^{-6})$ for $B^0 \rightarrow \omega\omega$ and $\mathcal{O}(10^{-7})$ for $B^0 \rightarrow \omega\phi$. The SM predicts longitudinal polarization fractions of $\mathcal{F}_L > 0.8$ for both modes [93,94]. Charmless vector vector modes are also well suited to measure the Unitarity Triangle angle α [96,97]. The Scan Method group has determined $\alpha - \beta$ contours from a χ^2 fit to measured branching fractions, longitudinal polarizations and CP asymmetries using all observed charmless vector vector decays [98]. The decay amplitudes of each mode are expressed in terms of tree, color-suppressed tree, gluonic penguin, singlet penguin, electroweak penguin and W -annihilation/ W -exchange amplitudes. For decays involving K^* s, $SU(3)$ breaking is taken into account. All contributions up to order $\mathcal{O}(\lambda^5)$ are considered where $\lambda = \sin \theta_c$ (Cabibbo angle), since the leading amplitude is already

at order $\mathcal{O}(\lambda^3)$. Figure 14 shows the 90% CL α - β contour determined from the fit.

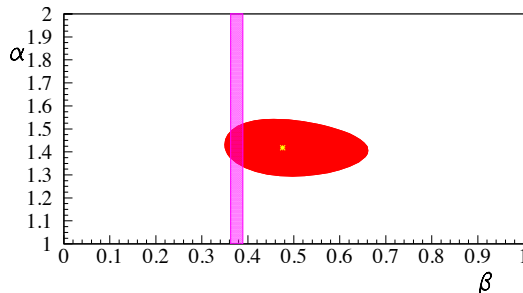


Figure 14. The α - β contour obtained from a ML fit to branching fractions, longitudinal polarizations and CP asymmetries measured in all observed $B \rightarrow VV$ modes. The magenta band shows the result of the $\sin 2\beta$ measurements in $B \rightarrow c\bar{c}K_{S,L}^0$ decays [77].

Using the full *BABAR* data sample of 471×10^6 $B\bar{B}$ events, we reconstruct the B -daughter candidates via their decays $\omega \rightarrow \pi^+\pi^-\pi^0$ with $\pi^0 \rightarrow \gamma\gamma$ and $\phi \rightarrow K^+K^-$ [99]. If multiple candidates exist, we select the one for which the χ^2 probability of a fit to the two vector meson masses is smallest. The combinatorial background from $e^+e^- \rightarrow q\bar{q}$ collisions dominates. We use a tight selection on the angle θ_T between the thrust of the B signal candidate in the $\Upsilon(4S)$ rest frame and that of the rest of the event, requiring $|\cos\theta_T| < 0.8$ (0.9) for $B^0 \rightarrow \omega\omega$ and $B^0 \rightarrow \omega\phi$ decay modes. Furthermore, we define a Fisher discriminant \mathcal{F} based on four shape and kinetic variables as inputs. We perform an extended unbinned ML fit to extract the signal and background yields from the data. We define the PDF as a product of six individual PDFs including m_{ES} , ΔE , \mathcal{F} , masses and helicity angles of the two vector mesons and the decay angle ψ between the π^0 in the dipion rest frame and the ω flight direction:

$$\mathcal{P}_j^i = \mathcal{P}_j(m_{ES}^i) \times \mathcal{P}_j(\Delta E^i) \times \mathcal{P}_j(\mathcal{F}^i) \times \mathcal{P}_j(m_{V_1}^i, m_{V_2}^i, \theta_1^i, \theta_2^i) \times \mathcal{P}_j(\psi_{\omega_1}^i) \times \mathcal{P}_j(\psi_{\omega_2}^i) \quad (6)$$

where the last term is not present in $B^0 \rightarrow \omega\phi$. For signal, we use a sum of two Gaussians for m_{ES} and ΔE , a two-piece normal distribution for \mathcal{F} , relativistic Breit-Wigner functions for the m_V distributions, each convolved with two Gaussians to account for detector resolution. We parameterize the helicity angles by the angular distribution:

$$W(\theta_{V_1}, \theta_{V_2}) \propto (1/4)(1 - \mathcal{F}_L) \sin^2 \theta_{V_1} \sin^2 \theta_{V_2} + \mathcal{F}_L \cos^2 \theta_{V_1} \cos^2 \theta_{V_2} \quad (7)$$

convolved with a resolution function for each angle. Thus for signal, the PDF is factorized as $\mathcal{P}_j(m_{V_1}^i, m_{V_2}^i, \theta_1^i, \theta_2^i) = \mathcal{P}_j(m_{V_1}^i) \times \mathcal{P}_j(m_{V_2}^i) \times W(\theta_{V_1}, \theta_{V_2})$. For the angles $\psi_{1,2}$, the PDFs are $\sin^2 \psi_{1,2}$ distributions. For combinatorial background, we use an Argus function [68] for m_{ES} , a second-order polynomial for ΔE and a two-piece normal distribution for \mathcal{F} . The masses and helicity angles of the two vector mesons are considered to be independent and thus are factorized. We use a third-order polynomial for the m_V distributions. The PDFs of the helicity angles are third-order polynomials for combinatorial background where the parameterization is obtained from on-peak sideband data ($m_{ES} < 5.27$ GeV/ c^2). Similarly, we use a third-order polynomial in $\cos\psi$ for the ω decay angle. We also consider $B\bar{B}$ peaking background determined from simulation. We parameterize m_{ES} , ΔE and \mathcal{F} with similar functions as those for the signal. The PDFs for m_V and ψ angle are similar to those of the combinatorial background. For the helicity angles, we use a fourth-order polynomial. For the signal, $B\bar{B}$ and $q\bar{q}$ background components, we determine the PDF parameters from simulation. We study large control samples of $B \rightarrow D\pi$ decays of similar topology to verify the simulated resolutions in ΔE and m_{ES} , adjusting the PDFs to account for any differences found.

Figures 15 (left, middle) show the m_{ES} and ΔE projections of the multidimensional ML fit for $B^0 \rightarrow \omega\omega$ (top) and $B^0 \rightarrow \omega\phi$ (bottom). Figure 15 (right) shows the corresponding distributions of $-2\ln(\mathcal{L}(B)/\mathcal{L}_0)$ for zero signal normalized to the likelihood at the minimum value for the two modes. We fix \mathcal{F} to 0.88 but vary it from 0.58–1.0 in the systematic error determination. Signal and background yields are extracted from the fit. For $B^0 \rightarrow \omega\omega$, we observe $N_{\omega\omega} = 69^{+16.4}_{-15.2}$ signal events. Including systematic uncertainties, this yields a 4.4σ effect. For $B^0 \rightarrow \omega\phi$, we see no signal. The fit yields $N_{\omega\phi} = -2.8^{+5.7}_{-4.0}$ signal events. Besides the uncertainty from the \mathcal{F}_L variation, systematic uncertainties include contributions from the PDF parameterization, selection efficiency, use of control samples, number of B mesons and B -daughter branching fractions. The largest systematic error comes from yield bias estimation in the fit yielding order $\mathcal{O}(5)$ events). We measure a branching fraction of $\mathcal{B}(B \rightarrow \omega\omega) = (1.2 \pm 0.3^{+0.3}_{-0.2}) \times 10^{-6}$, which agrees well with the SM prediction. We do not have enough data to measure \mathcal{F}_L in this mode. For the $B^0 \rightarrow \omega\phi$ mode, we set a Bayesian upper limit of $\mathcal{B}(B \rightarrow \omega\phi) = 0.7 \times 10^{-6}$ at 90% CL assuming a flat prior.

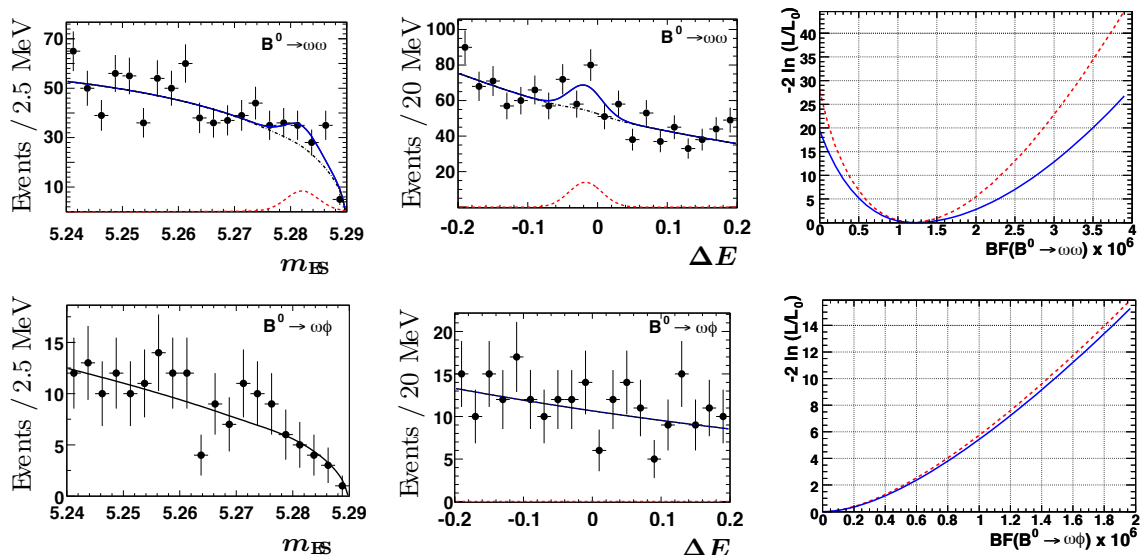


Figure 15. Fit results for $B^0 \rightarrow \omega\omega$ (top row) and $B^0 \rightarrow \omega\phi$ (bottom row) showing m_{ES} (left) and ΔE (middle) projections of the ML fit for data (points with error bars), the total PDF (solid blue line), background PDF (black dashed line) and signal contribution (red dashed line). The distributions of $-2\ln(\mathcal{L}(B)/\mathcal{L}_0)$ versus branching fraction (right) for statistical errors only (dashed red curve) and statistical and systematic errors combined (solid blue curve).

7. Conclusions

We have performed the most precise direct CP asymmetry measurement in the semi-inclusive $B \rightarrow X_s \gamma$ decay. The measurement error is still sufficiently large allowing to accommodate new physics contributions in the Wilson coefficient C_7^{eff} . We performed the first determination of $\text{Im}(C_8^{\text{eff}}/C_7^{\text{eff}})$ by measuring the difference in CP asymmetries between charged and neutral B decays. We measured partial branching fractions and CP asymmetries in $B \rightarrow X_s \ell^+ \ell^-$ that agree well with the SM predictions. We find no evidence for $B \rightarrow \pi/\eta \ell^+ \ell^-$ decays and set branching fraction upper limits at 90% CL that are a factor of two to three above the SM predictions. We also find no evidence for lepton number violation in $B^+ \rightarrow X^- \ell^+ \ell'^+$ decays and set stringent branching fraction upper limits at 90% CL. We find first evidence for $B^0 \rightarrow \omega\omega$ decays and measure a branching fraction that is consistent with the SM prediction. However, the

data sample is too small to extract \mathcal{F}_L from an angular analysis. We set an improved branching fraction upper limit at 90% CL for $B^0 \rightarrow \omega\phi$. Significant improvement on these measurements are expected to come from Belle II and for some decays also from LHCb.

8. Acknowledgment

This work has been supported by the Norwegian Research Council. I would like to thank the *BABAR* collaboration for the opportunity to give this talk. In particular, I would like to thank Justin Albert, Frank Porter, Fergus Wilson for useful comments.

References

- [1] K. Wilson, Phys. Rev. **179**, 1499 (1969); K. Wilson and J. Kogut, Phys. Rep. **12**, 75 (1974).
- [2] N. Isgur et al. Phys.Rev. **D 39**, 799 (1989); N. Isgur and M. Wise, Phys. Lett. B **232**, 113 (1989).
- [3] H. Georgi, Phys. Lett. B **240**, 447 (1990).
- [4] B. Grinstein and D. Pirjol, Phys. Rev. **D 70**, 114005 (2004).
- [5] G. Hiller and F. Krüger, Phys.Rev. **D 69**, 074020 (2004).
- [6] E. Majorana, Nuo. Cim. **14**, **171** (1937).
- [7] M. Misiak et al., Phys. Rev. Lett. **98**, 022002 (2007).
- [8] M. Misiak and M. Steinhauser, Nucl. Phys. **B 764**, 62 (2007).
- [9] M. Neubert, Phys. Rev. **D 72**, 074025 (2005).
- [10] B. O. Lange, M. Neubert, and G. Paz, Phys. Rev. **D 72**, 073006 (2005).
- [11] C. W. Bauer, et al., Phys. Rev. **D 67**, 054012 (2003).
- [12] P. Gambino et al., J. High Energy Phys. **10**, 058 (2007).
- [13] K.A. Olive et al., (Particle Data Group), Chin.Phys. **C 38**, 090001 (2014).
- [14] G. Eigen, arXiv:0907.4330 [hep-ex] (2009).
- [15] B. Aubert et al. (BABAR Collaboration), Nucl. Instrum. Meth. **A 479**, 1 (2002).
- [16] B. Aubert et al. (BABAR Collaboration), Nucl. Instrum. Meth. **A 729**, 615 (2013).
- [17] J.P. Lees et al. (BABAR Collaboration), Phys.Rev. **D 86**, 052012 (2012).
- [18] J.P. Lees et al. (BABAR Collaboration), Phys.Rev. **D 90**, 092001 (2014).
- [19] M. Benzke et al., Phys. Rev. Lett **106**, 141801 (2011).
- [20] B. Aubert et al. (BABAR Collaboration), Phys. Rev. Lett. **101**, 171804 (2008).
- [21] S. Nishida et al. (Belle Collaboration), Phys. Rev. Lett. **93**, 031803 (2004).
- [22] A. L. Kagan and M. Neubert, Phys. Rev. **D 58**, 094012 (1998).
- [23] M. Jung, X. -Q. Li and A. Pich, JHEP **1210**, 063 (2012).
- [24] A. Hayakawa, et al., Phys. Lett. **B 710**, 446 (2012).
- [25] J. P. Lees et al. (BABAR Collaboration), Phys. Rev. Lett. **109**, 191801 (2012).
- [26] J. P. Lees et al. (BABAR Collaboration), Phys. Rev. **D 86**, 112008 (2012).
- [27] B. Aubert et al. (BABAR Collaboration), Phys. Rev. **D 77**, 051103 (2008).
- [28] L. Pesantez et al. (Belle Collaboration), arXiv:1501.01702 [hep-ex] (2014).
- [29] T. E. Coan et al. (CLEO Collaboration), Phys. Rev. Lett. **86**, 5661 (2001).
- [30] T. Hurth, E. Lunghi and W. Porod, Nucl. Phys. **B 704**, 56 (2005).
- [31] J. P. Lees et al. (BABAR Collaboration), Phys. Rev. Lett. **112**, 211802 (2014).
- [32] T. Sjostrand, Comput. Phys. Commun. **82**, 74 (1994).
- [33] A. Ali, et al., Phys. Rev. **D 66**, 034002 (2002).
- [34] T. Huber, et al., Nucl. Phys. **B 740**, 105 (2006).
- [35] F. Krüger and L. M. Sehgal, Phys. Lett. **B 380**, 199 (1996).
- [36] A. Ali, et al., Phys. Rev. **D 55**, 4105 (1997).
- [37] C. Bobeth, M. Misiak, and J. Urban, Nucl. Phys. **B 574**, 291 (2000).
- [38] H. H. Asatryan et al., Phys. Rev. **D 65**, 074004 (2002).
- [39] H. H. Asatryan et al., Phys. Rev. **D 66**, 034009 (2002).
- [40] A. Ghinculov et al., Nucl. Phys. **B 648**, 254 (2003).
- [41] P. Gambino, M. Gorbahn and U. Haisch, Nucl. Phys. **B 673**, 238 (2003).
- [42] A. Ghinculov et al., Eur. Phys. J. **C 33**, S288 (2004).
- [43] C. Bobeth et al., JHEP **0404**, 071 (2004).
- [44] A. Ghinculov et al., Nucl. Phys. **B 685**, 351 (2004).
- [45] C. Greub, V. Pilipp and C. Schupbach, JHEP **0812**, 040 (2008).
- [46] T. Huber, T. Hurth and E. Lunghi, Nucl. Phys. **B 802**, 40 (2008).
- [47] M. Beneke, et al., Eur. Phys. J. **C 61**, 439 (2009).

- [48] B. Aubert et al. (BABAR Collaboration), Phys. Rev. Lett. **93**, 081802 (2004).
- [49] M. Iwasaki et al. (Belle Collaboration), Phys. Rev. **D 72**, 092005 (2005).
- [50] D. S. Du and M. Z. Yang, Phys. Rev. **D 54**, 882 (1996).
- [51] A. Ali and G. Hiller, Eur. Phys. J. **C 8**, 619 (1999).
- [52] C. Bobeth, G. Hiller and G. Piranishvili, JHEP **0807**, 106 (2008).
- [53] W. Altmannshofer, et al., JHEP **0901**, 019 (2009).
- [54] A. Soni et al., Phys. Rev. **D 82**, 033009 (2010).
- [55] A. K. Alok, A. Dighe and S. Ray, Phys. Rev. **D 79**, 034017 (2009).
- [56] T. M. Aliev and M. Savci, Phys. Rev. **D 60**, 014005 (1999).
- [57] J.P. Lees et al. (BABAR collaboration), Phys.Rev. **D 88**, 032012 (2013).
- [58] J. J. Wang, et al., Phys. Rev. **D 77**, 014017 (2008).
- [59] H. Z. Song, L. X. Lu, and G. R. Lu, Commun. Theor. Phys. **50**, 696 (2008).
- [60] G. Erkol and G. Turan, Eur. Phys. Jour. **C 28**, 243 (2003).
- [61] J.T. Wei et al., Phys. Rev. **D 78**, 011101 (2008).
- [62] R. Aaij et al. (LHCb collaboration), JHEP **1212**, 125 (1212).
- [63] F. R. Klinkhamer and N.S. Manton, Phys. Rev. **D 30**, 2212 (1984).
- [64] A. Atre, T. Han, S. Pascali, and B. Zhang, JHEP **0905**, 030 (2009).
- [65] Y. Fukuda et al. (Super-Kamiokande Collaboration), Phys. Rev. Lett. **81**, 1562 (1998).
- [66] S. Davidson, E. Nardi and Y. Nir, Phys. Rep. **466**, 105 (2008).
- [67] J.P. Lees et al. (BABAR collaboration), Phys.Rev. **D 89**, 011102 (2014).
- [68] H. Albrecht et al. (ARGUS Collaboration), Z. Phys. **C 48**, 543 (1990).
- [69] K. S. Cranmer, Comput. Phys. Commun. **136**, 198 (2001).
- [70] T. Skwarnicki, DESY F31-86-02 (thesis, unpublished) (1986).
- [71] G. J. Gounaris and J.J. Sakurai, Phys. Rev. Lett. **21**, 244 (1968).
- [72] O. Seon et al. (Belle Collaboration), Phys. Rev. **D 84**, 071106 (2011).
- [73] R. Aaij et al. (LHCb Collaboration), Phys. Rev. Lett. **112**, 131802 (2014).
- [74] K. W. Edwards et al. (CLEO Collaboration), Phys. Rev. **D 65**, 111102 (2002).
- [75] P. del Amo Sanchez et al. (BABAR Collaboration), Phys. Rev. **D 83**, 091101 (2011).
- [76] J.P. Lees et al. (BABAR Collaboration), Phys. Rev. **D 85**, 071103 (2012).
- [77] D. Asner et al. (Heavy Flavor Averaging Group Collaboration), arXiv:1010.1589 [hep-ex] (2010).
- [78] C.W. Bauer et al., Phys. Rev. **D 70**, 054015 (2004).
- [79] P. Colangelo, F. De Fazio, and T.N. Pham, Phys. Lett. **B 597**, 291 (2004).
- [80] A.L. Kagan, Phys. Lett. **B 601**, 151 (2004).
- [81] M. Ladisa et al., Phys. Rev. **D 70**, 114025 (2004).
- [82] H. Y. Cheng, C. K. Chua, and A. Soni, Phys. Rev. **D 71**, 014030 (2005).
- [83] H.-N. Li and S. Mishima, Phys. Rev. **D 71**, 054025 (2005); Phys. Lett. B **622**, 63 (2005).
- [84] W. Bensalem and D. London, Phys. Rev. **D 64**, 116003 (2001).
- [85] A. K. Giri and R. Mohanta, Phys. Rev. **D 69**, 014008 (2004).
- [86] E. Alvarez et al., Phys. Rev. **D 70**, 115014 (2004).
- [87] C.-H. Chen and C.-Q. Geng, Phys. Rev. **D 71**, 115004 (2005).
- [88] Y.-D. Yang, R. M. Wang and G. R. Lu, Phys. Rev. **D 72**, 094002 (2005).
- [89] P. K. Das and K. C. Yang, Phys. Rev. **D 71**, 015009 (2005).
- [90] A. K. Giri and R. Mohanta, Eur. Phys. Jour. **C 44**, 249 (2005).
- [91] S. Baek et al., Phys. Rev. **D 72**, 094008 (2005).
- [92] S.-S. Bou et al., Phys. Rev. **D 77**, 095004 (2008).
- [93] Y. Li and C.-D. Lu, Phys. Rev. **D 73**, 014024 (2006).
- [94] H.-Y. Cheng and C.-K. Chua, Phys. Rev. **D 80**, 114008 (2009).
- [95] S. Oh, Phys. Rev. **D 60**, 034006 (1999).
- [96] D. Atwood and A. Soni, Phys. Rev. **D 59**, 013007 (1999); Phys. Rev. D **65**, 073018 (2002).
- [97] H.-W. Huang et al., Phys. Rev. **D 73**, 014011 (2006).
- [98] G. Eigen et al., Phys.Rev. **D 89**, 033004 (2014).
- [99] J.P. Lees et al. (BABAR collaboration), Phys.Rev. **D 89**, 051101 (2014).